The restricted random dislocation distribution model to describe ensembles of dislocations with a screw component in ZnO layers with a mosaic structure

R. Schifano, A. Wierzbicka, P. Dluzewski, et al.

COLLECTIONS

Paper published as part of the special topic on Defects in Semiconductors 2022

View Online   Export Citation   CrossMark

ARTICLES YOU MAY BE INTERESTED IN

Characterization methods for defects and devices in silicon carbide
Journal of Applied Physics **131**, 140903 (2022); https://doi.org/10.1063/5.0077299

Phonon study of Jahn–Teller distortion and phase stability in $NaMnO_2$ for sodium-ion batteries
Journal of Applied Physics **132**, 055101 (2022); https://doi.org/10.1063/5.0086903

Understanding interfacial energy structures in organic solar cells using photoelectron spectroscopy: A review
Journal of Applied Physics **132**, 050701 (2022); https://doi.org/10.1063/5.0091960

AIP Publishing

The restricted random dislocation distribution model to describe ensembles of dislocations with a screw component in ZnO layers with a mosaic structure

R. Schifano,[1,a)] A. Wierzbicka,[1] P. Dluzewski,[1] J. Z. Domagala,[1] W. Wozniak,[1] B. Kurowska,[1] C. Bazioti,[2] and E. Guziewicz[1]

AFFILIATIONS

[1]Institute of Physics, Polish Academy of Sciences, Al. Lotników 32/46, 02-668 Warsaw, Poland
[2]Department of Physics, Centre for Materials Science and Nanotechnology, University of Oslo, P.O. Box 1048, Blindern, N-0316 Oslo, Norway

Note: This paper is part of the Special Topic on Defects in Semiconductors.
[a)]**Author to whom correspondence should be addressed:** schifano@ifpan.edu.pl

ABSTRACT

By applying the restricted random dislocation distribution model, solved using a discrete Hankel transform approach, it is shown that the shapes and characteristics of the ω-scans of the ZnO 00.2 reflection are mainly determined by the strain field introduced by dislocations with a screw component. On the other hand, no clear evidence of mosaicity or interfacial region contributions is found despite the layers exhibiting a c axis oriented residual columnar structure and a highly defective interface being present. The applied model not only permits a more precise estimation of the densities of dislocations, which present a screw component with respect to methods based on the analysis of the 00.2 peak ω-scan FWHM, but also gives an indication of their distribution characteristics with the extracted values, as well as their homogeneous/quasi-regular spacing, being confirmed by cross-sectional transmission electron microscopy observations.

I. INTRODUCTION

ZnO is a wide bandgap ($\sim$3.4 eV at 300 K) semiconductor that has attracted increasing interest in the recent decades and has been investigated for the realization of ultraviolet photodiodes, chemical- and bio-sensors, thin film transistors, and piezoelectric transducers.[1–3] In addition, due to the possibility of tuning the resistivity as low as $\gtrsim 2 \times 10^{-4}\,\Omega\,\text{cm}$ while maintaining a high transparency in the visible spectrum, ZnO represents a valid alternative to indium tin oxide. That is, ZnO has similar properties to the latter but is less expensive since it is based on zinc that is more abundant than indium. Furthermore, it is possible to grow thin ZnO-based films with good structural, electrical, and optical properties using cost-effective and scalable deposition approaches like atomic layer deposition (ALD) and magnetron sputtering. This makes the use of ZnO particularly advantageous in the case of industrial applications where a large area has to be covered with a transparent electrode, as in the case of organic/inorganic solar cells and flat displays. Regarding these deposition techniques, detailed studies have reported, as an example, that films with a ω-scan full width at half maximum (FWHM$_\omega$) of the 00.2 peak equal to $\sim$40–70 and $\sim$250 arcsec can be obtained by radio frequency (RF) sputtering on hydrothermally grown ZnO wafers (Zn face)[4,5] and by ALD deposition on GaN substrates,[6] respectively, using overall substrates temperatures $\leq$500 °C. The low FWHM$_\omega$s obtained in the above-mentioned studies indicate layers of good crystal quality. In addition, they are within the range of values reported in the case of thin films grown by molecular beam epitaxy, chemical vapor deposition, and metalorganic chemical vapor deposition that are typically extending from $\sim$10 to $\sim$280 arcsec[7–10] (for a review see, as an example, Ref. 11).

To get more insight into the microstructural characteristics of the layer, in some of the above-mentioned studies and similar ones, the mosaicity[12,13] is generally *a priori* assumed as being the main factor determining the x-ray peak profiles. In detail, the films are considered to consist of single crystallites with average vertical and lateral dimensions corresponding to the vertical and lateral coherence lengths, respectively. Furthermore, the model assumes that the blocks can be misoriented in the in-plane and in the growth direction, and these deviations are defined as the mosaic twist and tilt, respectively. These misorientations and the block dimensions are assumed to be the key parameters affecting the x-ray peak profiles and are, therefore, extracted from the x-ray characterization. A similar approach, also previously employed in the case of RF-sputtered ZnO films,[4] appears to be the natural choice in the case of ALD-grown ZnO layers of high quality, considering that they generally present a *c* axis oriented residual columnar structure.[6,14]

The purpose of the present study is to show that, despite exhibiting a residual columnar structure, the strain field introduced by dislocations with a screw component represents the main contribution to the ω-scan of the ZnO 00.2 reflection. That is, by using the restricted random dislocation distribution (RRDD) model solved using a discrete Hankel transform approach that allows us to significantly simplify and improve the numerical solution of its analytical expression, it is possible to accurately reproduce the ω-scan of the ZnO 00.2 reflection. The cumulative densities of dislocations with a screw component, as well as their distribution characteristics so extracted, are confirmed by cross-sectional transmission electron microscopy (TEM) measurements.

II. EXPERIMENTAL DETAILS

Commercially available semi-insulating GaN on sapphire templates with 00.2 ω-scans presenting a FWHM$_\omega$ and curvature equal to $\sim$200 arcsec and $\sim$7 m, respectively, purchased from Kyma Technologies,[15] were first cleaned in acetone, isopropanol, and de-ionized (DI) water. Afterward, the substrates were dipped for 10 min in a $H_2O_2 + H_2SO_4$ solution and a buffered oxide etch solution with each of them followed by a DI water rinse. Then, the ZnO films were grown by ALD at 300 °C using diethylzinc (DEZn), DI water, and nitrogen as precursors for zinc, oxygen, and purging gas, respectively. The pulsing/purging times were set equal to 20 ms/20 s and 20 ms/8 s for the DEZn and DI water precursors, respectively. The number of cycles was chosen in order to achieve a thickness of $\sim$1.5 μm. Here, it is worth pointing out that the selected growth temperature, while being out of the ALD growth window that is extending from $\sim$110 to $\sim$170 °C,[16,17] is still below the maximum temperature reported for the growth of ZnO using DEZn and DI water as precursors (325 °C in Ref. 18). Furthermore, it is the onset temperature for the DEZn pyrolysis;[19] hence, it is the upper temperature limit for avoiding substantial DEZn fragmentation.

Post-deposition annealing at 400, 600, and 800 °C for 30 min in N_2 flow was performed on selected samples. Survey θ–2θ x-ray diffraction measurements of these layers, in addition to those in the as-grown state, were performed using a Panalytical X'Pert Pro MRD diffractometer equipped with a hybrid two-bounce Ge (220)

monochromator in order to select the CuKα_1 line and Soller slits in front of a Pixcel detector. Reciprocal scan maps (RSMs) were acquired with the same diffractometer equipped with a hybrid two-bounce Ge(220) monochromator and a three-bounce Ge(220) analyzer in front of a proportional detector. Then, the structural characteristics were investigated further with a high-resolution Philips X'Pert diffractometer equipped with a four-bounce Ge(022) asymmetric monochromator placed on the primary beam side and a three-bounce Ge(220) analyzer introduced in the path of the diffracted beam. With this setup, 2θ-ω and 00.2 transverse ω-scans were acquired, and these latter are collectively referred to as high-resolution x-ray diffraction (HXRD) measurements throughout the article. The high-resolution Philips X'Pert diffractometer instrumental resolution was checked using a commercially available 1×1 cm ammonothermal GaN wafer.[20] The 00.2 FWHM$_\omega$ was found to be equal to 23 arcsec and is included in the 00.2 FWHM$_\omega$ uncertainties given throughout the present report. Successively, lamellae were prepared by ion milling using a FEI Helios-Nanolab and were reduced to a thickness of (70 ± 30) nm, as measured during their preparation. In order to analyze the overall crystal quality and the substrate–film interface characteristics, bright-field TEM and HR-TEM imaging were carried out on the cross-sectional lamellae with a FEI Titan Cubed 80-300 instrument operated at an acceleration voltage of 300 kV. For the observation of the dislocations, cross-sectional two-beam dark-field images with diffraction vector, **g**, equal to $< 00.2 >$ were acquired using the same instrument. The dislocation densities were extracted from the analysis of film sections extending $\geq$17 μm in the ZnO/GaN interface direction.

III. DETAILS ON THE ANALYSIS AND EXPERIMENTAL RESULTS

The remainder of this report is organized as follows: in Sec. III A, it shown that the layers investigated are only slightly tensile strained and exhibit a highly *c* axis oriented residual columnar structure. Then, in Sec. III B, the RRDD model is introduced. In addition, details concerning the numerical approach used for solving the analytical expression that describes the expected shape of the ω-scans are given. In the same subsection, the application of the RRDD model to the 00.2 ω-scan of the as-grown layer is discussed. Furthermore, since the TEM characterization performed on the as-grown layer also revealed the presence of a highly defective interfacial layer that could potentially affect the 00.2 ω-scans significantly, in order to strengthen the validity of the results, layers annealed up to 800 °C were also analyzed. These results are presented in Sec. III C. Finally, in Sec. III D, the densities of dislocations so obtained and confirmed by TEM observations are compared with those extracted using only the FWHM$_\omega$, as commonly done in the literature.

A. Overall structural characteristics of the as-grown layers

The comparison between survey θ–2θ scans of the substrate and the full structure including the ZnO film is shown in Fig. 1(a). No indications of any additional peak beside the 00.2 reflection and its 00.4 replica originating from the ZnO layer and almost
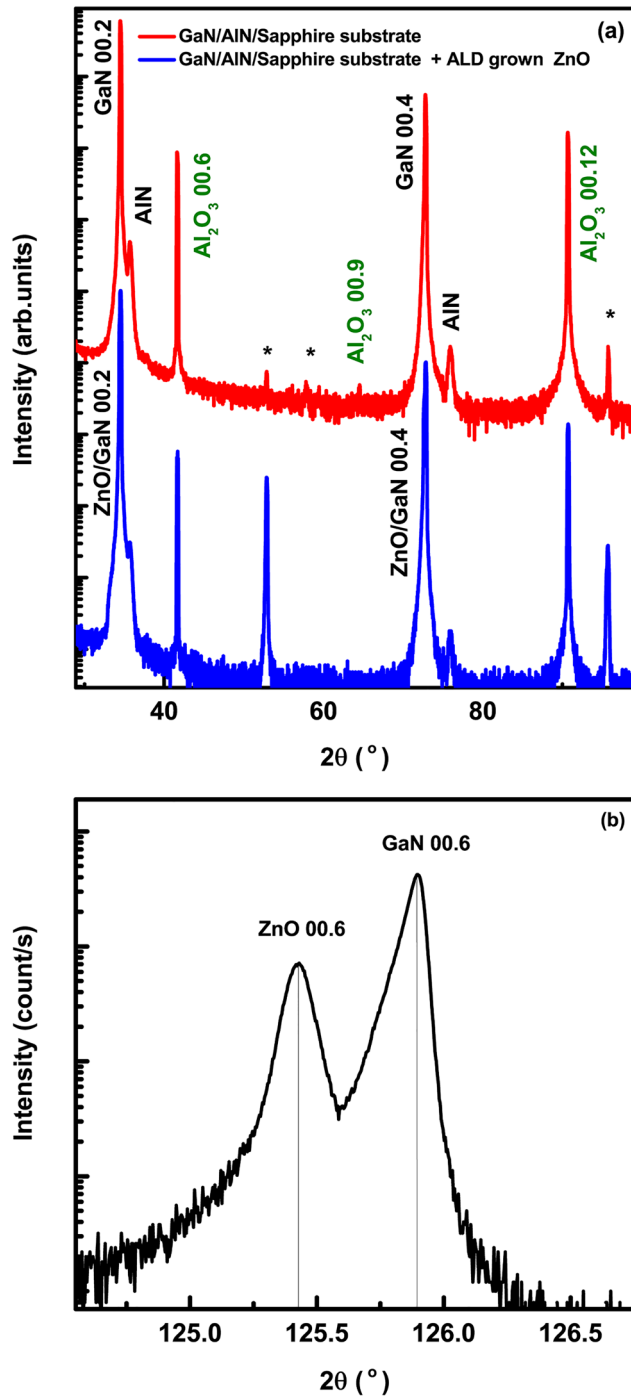
FIG. 1. (a) Survey θ-2θ diffraction pattern of the GaN on the sapphire substrate (red) and GaN on the sapphire substrate with the ZnO film on top (blue). The Miller indices corresponding to the peaks, as well as the material from which they are originating from, are also indicated in the figure. The asterisks indicate additional peaks originating from the substrate with multiple/uncertain attribution. (b) 2θ-ω scan showing the ZnO 00.6 peak resolved from that of the GaN substrate.

overlapping with those of GaN are present, with the remaining peaks being related to sapphire and the AlN buffer layer introduced at the GaN/sapphire interface.[15] On the other hand, a 2θ-ω scan used to resolve the 00.6 ZnO peak from that of the GaN substrate is shown in Fig. 1(b). From this symmetrical reflection and the $\bar{1}\bar{1}.4$ asymmetrical peak position (see Fig. 2 for a RSM including both the ZnO film and GaN substrate contributions), and neglecting the corrections for refraction effects due to the difference in refractive index between the sample and air,[21] the c and a lattice constants have been evaluated and found equal to (5.2004 ± 0.0002) and (3.2531 ± 0.0007) Å, respectively. These lattice constants correspond to strain values $\epsilon_c = (c - c_0)/c_0 \sim -0.12\%$ and $\epsilon_a = (a - a_0)/a_0 \sim 0.10\%$, where c_0 and a_0 are the single crystal ZnO lattice parameters (5.2066 and 3.2498 Å, respectively, taken from Ref. 22). This implies that the layer is only in-plane slightly tensile strained and contracted in the c direction as also suggested by the RSM shown in Fig. 2. The presence of strain is compatible with the difference in thermal expansion coefficient between the ZnO layer and the substrate, i.e., thermally induced biaxial strain. On the other hand, TEM observations, as the one shown in Fig. 3, reveal the presence of regions with darker tones extending in the growth direction from the ZnO/GaN interface toward the dips on the surface. Examination by HR-TEM of this portion of the sample suggests incoherent boundaries between the two parts of the film lying on opposite sides with respect to the defective line originating from the dip, as shown in Fig. S1(a) in the supplementary material. Moreover, a fast Fourier transform analysis of the acquired HR-TEM images provided evidence of a $\lesssim 1°$ in-plane misorientation between these two blocks [see Figs. S1(b) and S1(c) in the supplementary material]. That is, the film presents a residual columnar structure as anticipated by previous reports.[6,14] The average column width
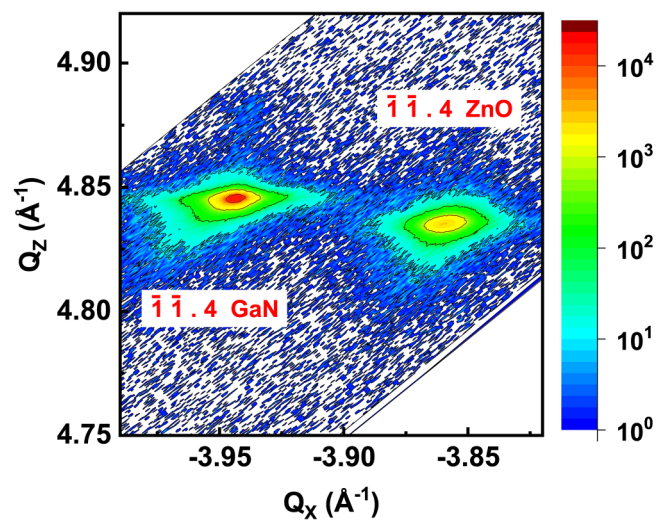

FIG. 2. Reciprocal scan map, RSM, relative to the $\bar{1}\bar{1}.4$ reflections originating from the as-grown ZnO layer and the GaN substrate with the color bar indicating the counts per seconds. Q_x and Q_y are in $2\pi/a$ and $2\pi/c$ units, respectively.
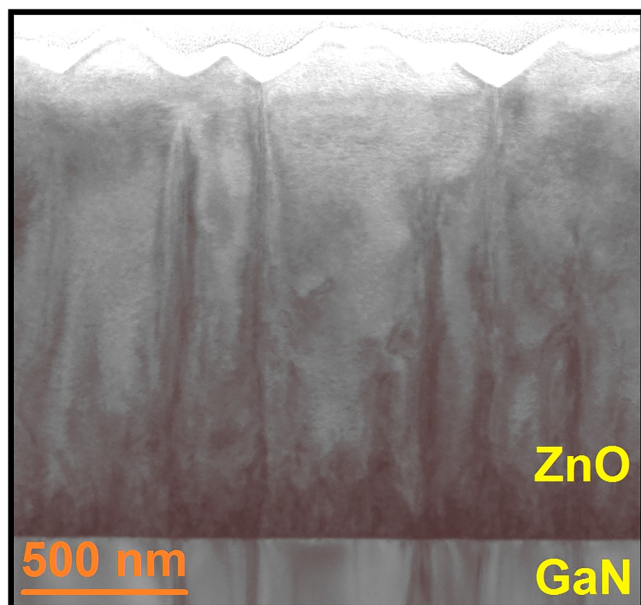
FIG. 3. Bright-field TEM image of the overall film cross section taken along the [11.0] zone axis.

FIG. 4. Experimental 00.2 transverse ω-scan (blue circles) and the best fitting Voigt profile (red line). The fit to the intensity profile assuming a RRDD [Eq. (2)] as well as the ω^{-4} asymptotic behavior expected for such a model are also displayed as black and green curves, respectively. In the inset, the same experimental data, Voigt function, as well as fit curve are shown in a log-linear scale instead. In the case of the fit curve, a background level of 1 count/s was added to Eq. (2).

was calculated on the basis of the dips occurrence in TEM bright-field images such as the one shown in Fig. 3 and found equal to (220 ± 50) nm in the present films. This combined with the absence of other reflections in exception of the 00.2 peak and its replica in the case of the θ–2θ scan and the 00.2 FWHM$_\omega$ equal to (260 ± 30) arcsec (see the inset of Fig. 4) excludes a large c axis columnar misorientation.

To summarize, overall, in the as-grown state, the layers exhibit structural characteristics that are close to those previously reported for high crystal quality ZnO films deposited by ALD on GaN substrates in similar growth conditions;[6,23–25] that is, they are slightly tensile strained with a highly c axis oriented columnar structure for that matter defined residual columnar structure in the present work.

B. The RRDD model in the as-grown layer case

As mentioned in the Introduction, to extract further information from the XRD measurements concerning the structural characteristics of layers similar to those analyzed here, the mosaicity is generally *a priori* postulated as the key factor determining the ω-scan profile. In this case, the layer is modeled as an agglomerate of good crystal quality building blocks that are essentially free of dislocations with a distribution of geometrically necessary dislocations located between the blocks to account for the relative misorientations among them.[12,13] Furthermore, if for the sake of simplicity we limit our discussion to symmetric ω-scans, it is implicitly assumed that the total integral breadth of these peaks is the sum of the tilt and lateral coherence length broadening. That is, the two contributions are assumed to be independent and can, therefore, be separated using a
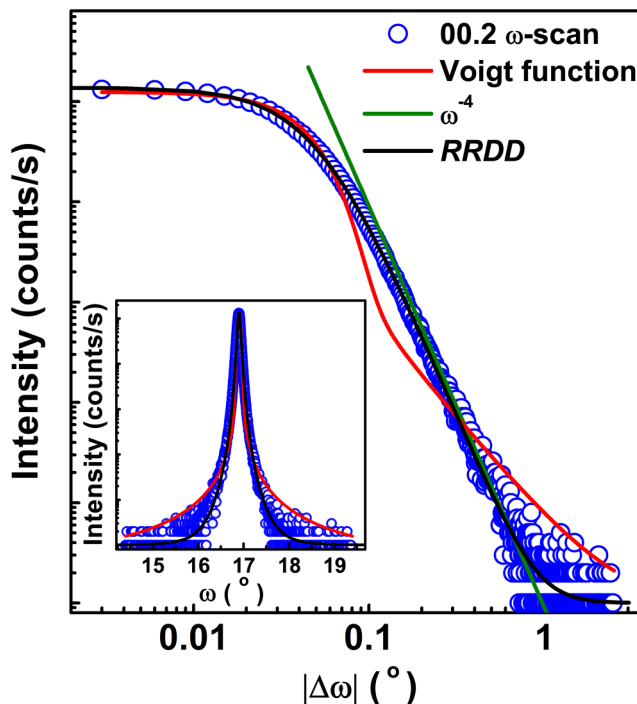
Williamson–Hall-like plot.[26] However, the limited lateral coherence length, due to dimensional fluctuations, leads to a Lorentzian profile.[27] On the other hand, a random rotational misorientation distribution can be assumed. This results in a Gaussian probability distribution for the mosaic blocks as a consequence of the central limit theorem and, accordingly, in a Gaussian peak shape. Therefore, the profile of a mosaic structure is anticipated to be, in the above approximations, a convolution of a Gaussian and a Lorentzian profile, i.e., a Voigt function. Hence, line profile analysis, originally developed for powder samples[28,29] or further evolutions,[30,31] can be equally used to separate the contribution of the tilt and of the lateral coherence length to the peak broadening, with previous reports providing evidence that the two methods are equivalent.[4,26] In the present case, however, it has been found that the 00.2 transverse ω-scan cannot be accurately reproduced with a Voigt profile as shown in Fig. 4 and in the inset of the same figure, where a log–log and log-linear plot of the 00.2 ω-scan are compared with the Voigt profile minimizing the χ^2 (red curve), respectively. This, despite the as-grown layers, as thoroughly shown in Subsection III A, present a highly c axis oriented columnar structure with in-plane misorientation; therefore, assuming that the mosaicity is the key factor that determines the 00.2 ω-scan profile characteristics seems to be the

obvious choice. On the other hand, it is evident from the displayed data that the tail of the measured peak, i.e., the scattered intensity, rather follows the ω^{-4} asymptotic law. This corresponds to the dependence expected for the strain field introduced by a restricted random distribution of dislocations.[32,33] In the RRDD model, the term "restricted" was first proposed by Wilkens in Ref. 34. It underlines the assumption that the total distribution of dislocations can be subdivided into groups crossing equally sized circles orthogonal to the direction of the dislocations. Within each group, the same amount of dislocations with opposite Burgers vectors is present and is distributed randomly but independently from the other areas. That is, it is based on the introduction of the correlation length, L, being the radius of the characteristic circles. This approach is applied here to quantitatively analyze the 00.2 ω-scan and to obtain the key parameters characterizing the ensemble of dislocations. Dislocations found in ZnO, similar to other wurtzite-type materials, are pure screw, pure edge, and mixed; they are characterized by the Burgers vectors $\boldsymbol{b}_S = <0001>$, $\boldsymbol{b}_E = 1/3 <11\bar{2}0>$, and $\boldsymbol{b}_M = 1/3 <11\bar{2}3> = \boldsymbol{b}_S + \boldsymbol{b}_E$, respectively.[35] However, in the symmetric configuration, the measured profiles are sensitive only to dislocations with at least a component of the Burgers vector parallel to the diffraction vector, $\boldsymbol{Q}$, i.e., threading screw or mixed-type dislocations that are in this configuration indistinguishable. Then, if the screw/mixed dislocations are assumed to extend over the whole layer and the instrumental broadening and curvature are neglected, since introducing a total correction $\sim$10% to the measured FWHM$_\omega$, the intensity $I(\boldsymbol{q})$ of a symmetric ω-scan as a function of $\boldsymbol{q}$, the deviation from the corresponding $\boldsymbol{Q}$ in the plane orthogonal to it, is described by[32,33]

$$I(\boldsymbol{q}) \propto \int_{\mathbf{R}^2} e^{i(q_x x + q_y y)} e^{-T(\rho)} \, dx \, dy, \quad (1)$$

with

$$T(\rho) = n_S \frac{(\boldsymbol{Q}\boldsymbol{b}_S)^2}{8\pi} \rho^2 \ln\left(\frac{L_S + \frac{\boldsymbol{Q}\boldsymbol{b}_S}{2\pi}\rho}{\frac{\boldsymbol{Q}\boldsymbol{b}_S}{2\pi}\rho}\right),$$

where n_S and L_S are the cumulative screw and mixed dislocation density and their overall correlation length, respectively, while $\rho = \sqrt{x^2 + y^2}$ with the xy-plane being the sample surface. Using polar coordinates, the expression for $I(\boldsymbol{q})$, as already reported in Ref. 36, can be further simplified to

$$I(q) \propto \int_0^\infty \int_0^{2\pi} e^{-iq\rho\cos(\theta-\alpha)} e^{-T(\rho)} \rho \, d\rho \, d\theta = 2\pi \int_0^\infty \rho J_0(q\rho) e^{-T(\rho)} \, d\rho, \quad (2)$$

where α is the angle between $\boldsymbol{q}$ and the reference direction of the polar reference system and $J_0(q\rho)$ is the zero-order Bessel function. That is, the peak profile as a function of q is the zero-order Hankel transform of the correlation function $e^{-T(\rho)}$. Hence, by setting $b_S = c$, remembering that $q = \frac{4\pi}{\lambda}\sin\omega\sin\theta_B$, with λ and θ_B being the CuKα_1 wavelength and the Bragg angle, respectively, the entire ω-scan peak profile can be fitted. Here, it is important to stress that besides the overall not so common use of the RRDD model in the

literature, previous reports[32,37] privileged the analysis of the rocking curves (RCs) instead. In this case, considering that a RC is an ω-scan acquired with an open detector and, therefore, represents an integrated measurement around the diffracted beam, the expected profile can be obtained by properly integrating Eq. (1). This implies the reduction of the Hankel transform to a Fourier transform.[32] However, in our case, the film is almost lattice matched with the substrate; hence, the 00.2 RCs inevitably include contributions from both the film and the substrate that, therefore, cannot be independently analyzed. That is, in similar situations, the approach described in detail herein and based on the zero-order Hankel transform of the correlation function $e^{-T(\rho)}$ should be used. In this case, the expected peak shape of $I(q)$ mathematically justifies the reduction of the Hankel transform integral to a Fourier–Bessel series. That is, the zero-order Bessel function orthogonal expressions are used as a basis, while the linear expansion coefficients are proportional to the values of $e^{-T(\rho)}$ sampled over the zero-order Bessel function zeros scaled appropriately. In this way, the integral is reduced to a discrete Hankel transform. Such methodology has been recently numerically tested and shown to be sufficiently accurate in the case of functions decaying as low as ρ^{-1}.[38,39] Likewise, a discrete Hankel transform approach has been employed here. It is worth pointing out that, despite numerical integration can be used instead,[40] this approach converges significantly faster than the ordinary quadrature integration. As an example, in our case, $e^{-T(\rho)}$ was sampled over 1024 points to obtain the presented fitting curves, while a direct numerical integration based on the midpoint values requires 10^4 points for each of the q values selected to obtain an accuracy equal to $\sim$1% with respect to the Hankel transform results.

Coming back to Eq. (2), from the fit of the ω-scan, the relevant quantities of the model, i.e., n_S and L_S, were extracted. As shown in Fig. 4, a remarkable agreement between the measured 00.2 transverse ω-scan and the simulated curve was achieved for $n_S = (3 \pm 1) \times 10^9 \, \text{cm}^{-2}$ and $L_S = (200 \pm 70)$ nm, with the latter being similar to the column width. Here, it is worth pointing out that the two fitting parameters are to a certain extent interdependent, as a close look to the expression of $T(\rho)$ reveals. Furthermore, both of them contribute, even though with different weights, to the resulting FWHM$_\omega$ (for more details, see Ref. 33). This dependency has been taken into account and results in the uncertainties reported above. Finally, the dimensionless parameter M_S, defined as $L_S\sqrt{n_S}$, was calculated and found equal to (1.2 ± 0.2). Considering that $1/\sqrt{n_S}$ represents the mean distance between dislocations with a screw component and L_S is the correlation length, i.e., the characteristic length that corresponds to the area containing the same density of dislocations with opposite Burgers vector, M_S should be ≥ 1 in order for the RRDD model to be applied; in the present case, therefore, the condition for approximating the dislocation ensemble as a RRDD is *a posteriori* verified. Finally, it is worth underlining that $L_S \sim 1/\sqrt{n_S}$ implies that the dislocations are homogeneously/quasi-regularly distributed.

To substantiate this analysis, cross-sectional dark-field TEM observations in two-beam conditions were performed with $\boldsymbol{g} = <00.2>$. In this configuration, considering the above-mentioned extinction criterion, similarly to the XRD case, screw and mixed threading dislocations are visualized with an example shown in Fig. 5. Hence, the cumulative density of dislocations
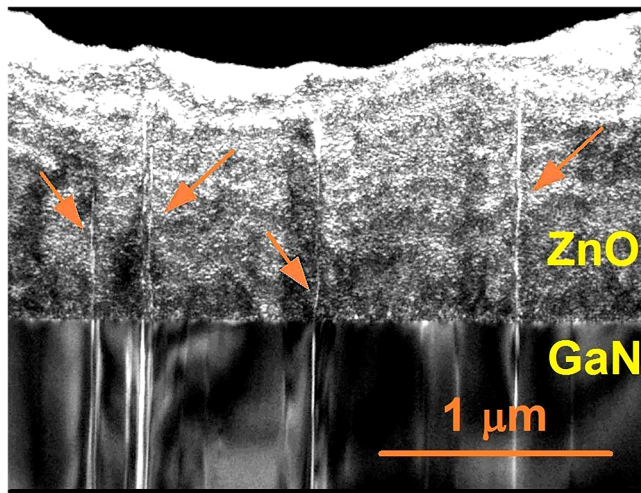
FIG. 5. Two-beam dark-field image taken with $\mathbf{g} = <00.2>$ with four visible dislocations indicated by arrows.

presenting a component of the Burgers vector parallel to $\boldsymbol{c}$, n_S^{TEM}, can be independently determined, if the thickness of the lamellae is known, and directly compared with n_S. Indeed, within the error ranges, agreement was found between the HXRD and TEM estimates, with the latter being equal to $(3 \pm 2) \times 10^9 \text{ cm}^{-2}$. This finding supports the model used herein to describe the screw and mixed dislocation distribution. It is worth pointing out that the error in n_S^{TEM} given above, as well as the error bars concerning it in Fig. 9(b), takes into account not only the statistical uncertainty related to the fluctuations in the dislocations number depending on the different two-beam dark-field images analyzed but also the systematic error due to the lamellae wedge shape with thickness decreasing from ~100 nm at the ZnO/GaN interface to ~40 nm at the film surface (cf. Sec. II).

Overall, the TEM images of the film cross section suggest that a large part of the dislocations threading into the film originate from the GaN substrate, with only <20% of them being generated at the interface between the GaN substrate and the ZnO layer. Second, the majority of the dislocation lines are found not to deviate considerably from the normal to the layer. Note that in some cases, they do not extend over the entire thickness of the ZnO part of the lamellae, as a close look at Fig. 5 reveals. This can be related, as an example, to the above discussed lamellae wedge shape and/or the mixed nature of some of the observed dislocations, since in the latter case, the dislocation lines are indeed expected to deviate 11°–16° from the c-direction.[45–47] Finally, the TEM analysis confirms that the dislocations are fairly homogeneously distributed in the ZnO film, a finding that is consistent with M_S being ~1.

The TEM characterization also revealed the presence of a highly defective GaN/ZnO interfacial region, as a close look at Fig. 3 suggests [see also Fig. S2(a) in the supplementary material]. A detailed analysis of the GaN/ZnO interface based on the intensity profiles in the growth direction extracted from TEM images, as

the one shown in Fig. 3, indicates that the region with reduced crystallinity is ~200 nm thick [for a representative intensity profile, see Fig. S3(a) in the supplementary material]. Overall, the low intensity of this part of the ZnO film points to a highly defective region with the randomness of the extended defects most probably contributing to their annihilation and coalescence. This promotes the growth of a layer with better crystal quality at distances ≳200 nm from the interface where the majority of defects are those that extend in the growth direction like threading dislocations and column boundaries. The above discussion can quantitatively explain the observed layered structure of the film; however, modeling its contribution to the measured HXRD peaks is clearly not an easy task due to its intrinsic structural complexity. In previous works dedicated to GaN layers grown on 6H-SiC and on AlN/sapphire,[32,37] the interfacial region was reduced to the misfit dislocations distribution that is required to release the lattice mismatch and its contribution was calculated accordingly. However, in this study, it was found that the film is strongly strained and defective at the interface [see Figs. S2(a) and S2(b) in the supplementary material]. That is, no evidence for the presence of misfit dislocations, corresponding to a relaxed structure, was found during the TEM analysis, with previous works also not being conclusive regarding their presence.[14] Therefore, the above-mentioned approach to analytically evaluate this contribution cannot be used here. On the other hand, in our case, both the limited crystallinity of the interfacial layer and its thickness, that is, only ~13% of the total, are consistent with what suggested by the results discussed above, i.e., its presence has a negligible impact on the 00.2 peak ω-scan characteristics. Further experimental proofs of its negligible impact are provided in Subsection III C.

C. The RRDD model applied to the annealed samples

A similar analysis based on the comparison of HXRD measurements and TEM observations was also performed on the annealed samples, and the results are discussed in this subsection. As shown in Figs. 6(a)–6(c), in the case of the layers annealed at 400, 600, and 800 °C as well, the RRDD model permits us to reproduce quite accurately the 00.2 ω-scans, with M_S varying in the ~1–2 range. The extracted n_S values are reported in Fig. 9(b) where for completeness the cumulative screw and mixed dislocation density corresponding to the as-grown layer is also added. In the same figure, n_S^{TEM}, as obtained from the analysis of dark-field TEM images with exemplifying cases displayed in Figs. 7(a)–7(c), is also plotted for comparison. It can be seen that agreement is found between the two estimates, thus, providing further support for the used approach. Furthermore, the M_S values suggest, in the case of the annealed samples as well, a homogeneous/quasi-regular dislocation distribution; a finding that is consistent with the TEM acquired images, which additionally confirm that the majority of dislocations thread from the substrate.

As in the case of the as-grown sample, TEM cross-sectional observations like those shown in Figs. 8(a)–8(c) were used to perform an intensity profile analysis of the GaN/ZnO interface, and the results are displayed in Fig. 9(a) [for a representative intensity profiles, one for each of the annealed samples, see Figs. S3(b), S3(c) and S3(d) in the supplementary material]. In detail, it was found
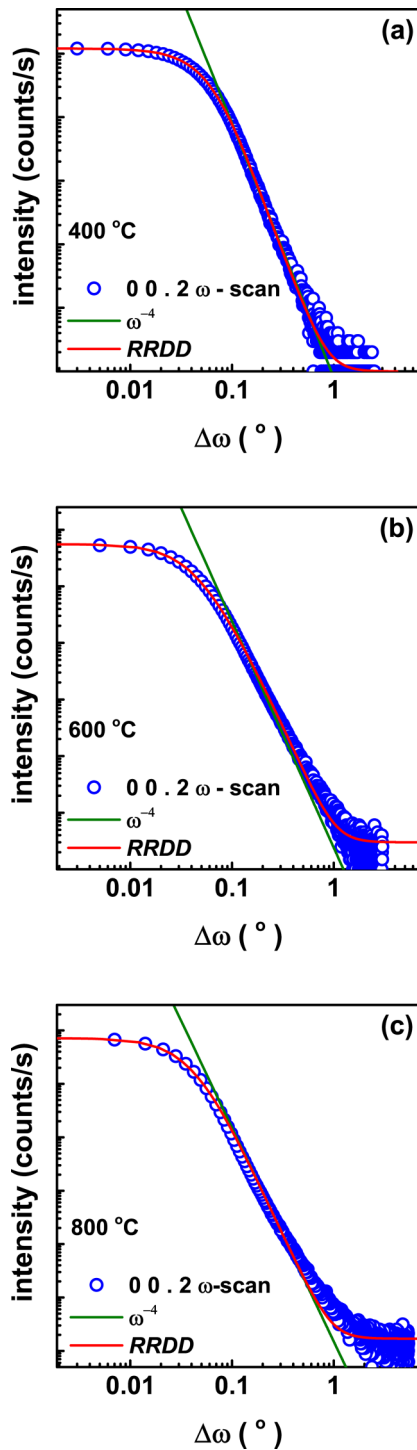
FIG. 6. In (a)–(c), the blue circles indicate the experimental 00.2 ω-scan for the samples annealed at 400, 600, and 800 °C, respectively. In each case, the corresponding fit assuming a RRDD as well as the ω^{-4} asymptotic behavior expected for such a model are displayed as red and green curves, respectively.
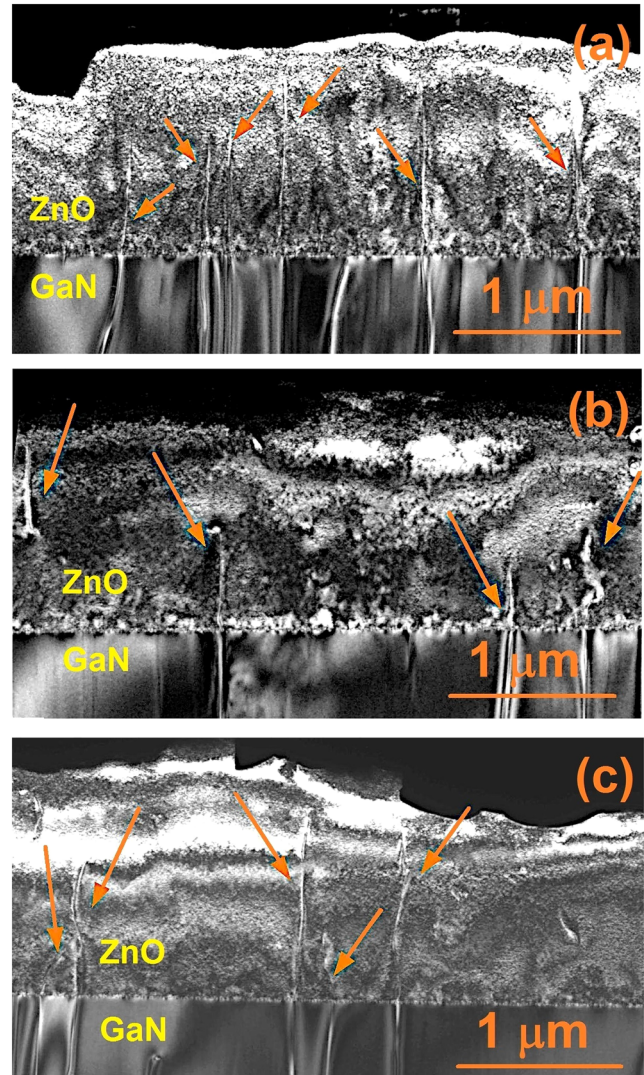

FIG. 7. (a)–(c) Representative dark-field images of the samples annealed for 30 min in N_2 flow at 400, 600, and 800 °C, respectively, acquired under two-beam dark-field conditions with $\mathbf{g} = <00.2>$. The observed dislocations are indicated by arrows.

that annealing at 400 °C reduces the thickness of the highly defective interfacial layer of factor 2 with another factor 2 reduction occurring after annealing at 600 °C with no further improvements in the interfacial structural quality following the final processing step. However, these changes do not correlate with the 00.2 $FWHM_\omega$s of the films that indeed follow the $FWHM_\omega$ fluctuations of the substrate, as shown in Fig. 9(a). In addition, considering that in the case of the annealed samples as well, no network of misfit dislocations was observed at the GaN/ZnO interface [see Fig. S2(b) in the supplementary material], we exclude a significant contribution of the highly defective interfacial layer to the 00.2 ω-scan
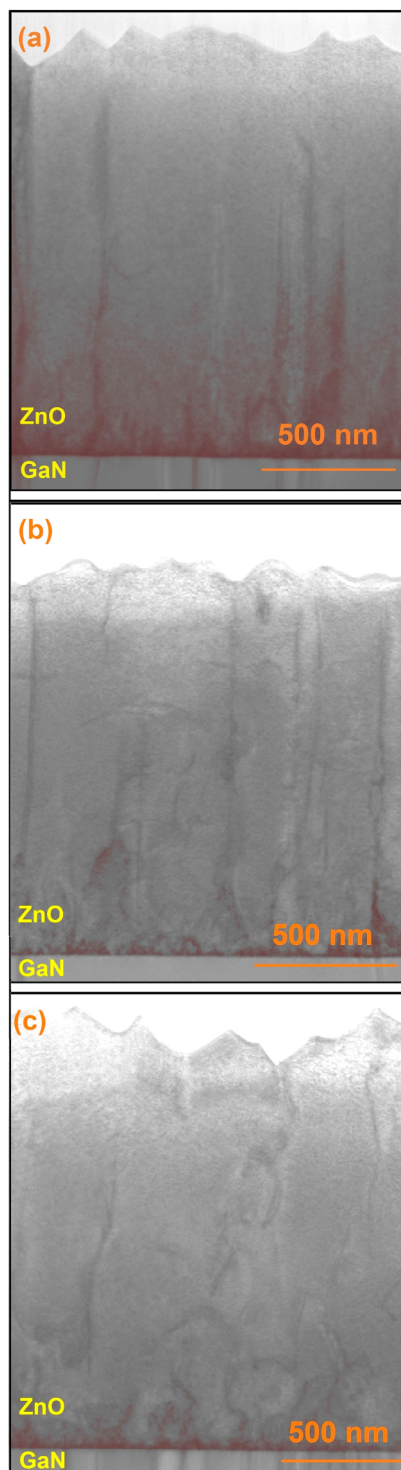
FIG. 8. (a)–(c) Representative cross-sectional bright-field TEM images relative to the samples annealed for 30 min in N_2 flow at 400, 600, and 800 °C, respectively. All the images were taken along the [11.0] zone axis.

peaks. This conclusion is further supported by the overall agreement found between n_S and n_S^{TEM}. In this respect, it is also worth pointing out that an n_S increase of $\sim 1.8 \times 10^9$ cm^{-2} corresponds to the FWHM$_\omega$ reduction of ~ 80 arcsec that was observed between the samples annealed at 400 and 600 °C. This is related to the above-mentioned interplay among the two fitting parameters n_S and L_S. In detail, in these samples, the cumulative dislocation density increment is counterbalanced by a decrease in L_S from (400 ± 100) to (160 ± 70) nm with the more than two times smaller L_S compensating for the larger n_S value. Similarly, despite the FWHM$_\omega$ of the sample annealed at 400 °C being ~ 20 arcsec larger than the as-grown one, the fit shown in Fig. 6(a) was achieved for $n_S = (2.4 \pm 0.5) \times 10^9$ cm^{-2} and $L_S = (400 \pm 100)$ nm with the two times larger L_S contributing to the $\sim 0.6 \times 10^9$ cm^{-2} lower value of n_S. That is, in the case of the RRDD model, due to the presence of the additional parameter L_S, the correlation between the dislocation density and the FWHM$_\omega$ is not as obvious as in the more commonly used approaches discussed in Subsection III D. In addition, it is worth pointing out that as evident from Figs. 7(b) and 7(c), in the case of the samples annealed at temperatures ≥ 600 °C, the presence of fragmented/not straight dislocations was observed in some of the acquired TEM images. Even though the limited statistic intrinsic in the TEM analysis does not permit a firm conclusion, this might suggest that temperatures ≥ 600 °C are required for the motion of dislocations with a screw component in ZnO to occur. Hence, in this respect, the observed n_S drop following the 800 °C processing step [see Fig. 9(b)] is possibly related to a real physical reduction of the cumulative screw and mixed dislocation density though within the experimental errors. On the contrary, the cross-sectional TEM imaging, with examples shown in Figs. 8(a)–8(c), suggests that recrystallization is occurring at ≥ 600 °C causing migration/deviation of the defective column boundaries from the growth direction and their correlated reduction. This could be, for example, the source of the increased diffuse scattering that causes the minor deviation from the ω^{-4} asymptotic law and to which corresponds the less accurate fitting of the ω-scan curve for $\Delta\omega \geq 0.2°$ that is observed in the case of the sample annealed at 800 °C [see Fig. 6(c)]. This attribution is supported by the fact that a similar discrepancy, even though to a lesser extent, is also present in the case of the 600 °C annealed sample as can be seen by a close look at Fig. 6(b). That is, its appearance is concomitant with the recrystallization onset. However, considering the satisfactory agreement found between the experimental curves and the RRDD model, a firm assignment of the physical source of this minor discrepancy is beyond the scope of the present work and will not be discussed further.

D. Comparison between the densities of dislocations with a screw component as extracted from the RRDD model and FWHM$_\omega$ based equations

Finally, it is worth comparing the n_S values with the cumulative screw and mixed dislocation densities extracted from the simple equations commonly used in the literature and for ZnO films as well,[41–43]

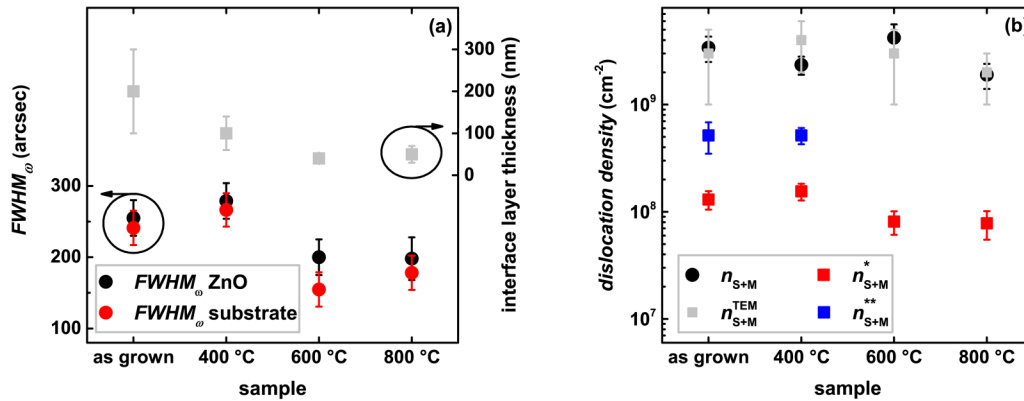$$n_S^\star = \frac{FWHM_\omega^2}{4.35\, b_S^2} \qquad (3)$$

FIG. 9. (a) Evolution of the thickness of the ZnO/GaN interfacial layer with limited crystallinity vs annealing temperature. In the same figure, the 00.2 ω-scan FWHM$_\omega$s of the ZnO films and corresponding GaN substrates are also reported. (b) The densities of dislocations with a screw component in the case of the as-grown and annealed samples as extracted from TEM imaging as well as evaluated from HXRD measurements assuming a RRDD. For comparison, the density estimates obtained from Eqs. (3) and (4) (the latter employed only in the case of the as-grown and 400 °C annealed samples) are also shown.

and

$$n_S^{**} = \frac{FWHM_\omega}{2.1\, b_S\, L}, \qquad (4)$$

where in Eq. (3) a random dislocation distribution and in Eq. (4) a piling up of dislocations in the grain boundary of length L are assumed to cause the tilting of the mosaic block, respectively. The comparison between both n_S^* and n_S^{**} and the estimates obtained according to the RRDD model is also shown in Fig. 9(b). It can be seen that n_S^* is smaller than n_S by at least a factor of ~15. On the other hand, if Eq. (4) is employed, the discrepancy reduces to a factor of 5. In this case, L has been set equal to the columnar width as determined by TEM imaging and extracted as described in Sec. III A; this rules out the reported underestimation occurring when a Williamson–Hall-like plot is used to evaluate L as it is commonly done.[21] However, the analysis has been limited to the as-grown and annealed at 400 °C samples only due to the occurrence of recrystallization observed above this temperature with the films losing their evident columnar structure. Here, it is worth underlining that the total FWHM$_\omega$ was actually used for calculating the values of both n_S^* and n_S^{**} displayed in Fig. 9(b) due to the above-mentioned impossibility of accurately fitting the peaks with a Voigt function. On the contrary, a proper analysis requires using only the Gaussian related contribution to the 00.2 peak width, since is the component related to the blocks tilting if the film is modeled as mosaic-structured, as discussed in detail above. That is, overall both the n_S^* and n_S^{**} values so calculated rather represent upper bounds.

In conclusion, the method shown here and based on the RRDD model with the 00.2 ω-scan simulated using a discrete Hankel transform approach permits us to accurately reproduce the experimental HXRD profiles and to properly evaluate the density of dislocations presenting a screw component (i.e., screw or mixed dislocations), with the extracted values being confirmed by TEM measurements.

On the other hand, estimates based on the FWHM$_\omega$ provide ~1 order of magnitude lower densities as proven in the case of GaN layers grown on 6H-SiC as well.[32] That is, albeit even more advanced models than the RRDD approach have been proposed (for a review, see, for example, Chap. 11 in Ref. 44), this procedure is sufficient for a correct description of ALD-grown ZnO films despite presenting a residual columnar structure and a highly defective interface. Finally, on the basis of the extracted correlation length, it can be concluded that the dislocations with a screw component are homogeneously/quasi-regularly distributed within the samples regardless of the post-deposition annealing temperature if ≤ 800 °C, a finding that is consistent with the TEM images acquired.

IV. CONCLUSIONS

In this work, it has been displayed, by combining TEM and HXRD measurements performed on high crystal quality ALD-grown ZnO films deposited on GaN/sapphire substrates, that an analysis based on the restricted random dislocation distribution model should be performed if an accurate estimate of the dislocation densities is required. In detail, it has been shown that within this model, it is possible to accurately reproduce the 00.2 ω-scan curves, even though the films exhibit a residual columnar structure. This indicates that the strain related to the dislocations presenting a screw component (i.e., screw or mixed dislocations), which mainly originate from the substrate, represents the main contribution that affects the ω-scan characteristics in the case of symmetric 00.2 peaks. On the other hand, the remaining possible sources like column boundaries, column–column interactions, the highly defective layer present at the ZnO/GaN interface, as well as mosaicity effects like tilt and limited size effects, have a negligible impact. Annealing the films for 30 min in N$_2$ flow up to 800 °C is found to have a minor effect on the density of dislocations with a screw component, while recrystallization with the reduction/migration of the defective column boundaries occurs with annealing temperatures ≥ 600 °C.

SUPPLEMENTARY MATERIAL

See the supplementary material for more details concerning the TEM analysis, i.e., for Figs. S1(a)–S1(c), S2(a) and S2(b), and S3(a)–S3(d).

AUTHOR DECLARATIONS

Conflict of Interest

The authors have no conflicts to disclose.

Author Contributions

R. Schifano: Conceptualization (lead); Data curation (lead); Formal analysis (equal); Funding acquisition (equal); Project administration (lead); Investigation (equal); Methodology (lead); Resources (equal); Software (lead); Validation (equal); Visualization (equal); Writing – original draft (lead); Writing – review and editing (equal). **A. Wierzbicka:** Formal analysis (equal); Investigation (equal); Validation (equal); Visualization (equal); Writing – original draft (supporting); Writing – review and editing (equal). **P. Dluzewski:** Formal analysis (equal); Investigation (equal); Methodology (supporting); Validation (equal); Visualization (equal); Writing – original draft (supporting); Writing – review and editing (equal). **J. Z. Domagala:** Formal analysis (equal); Investigation (equal); Validation (equal); Visualization (equal); Writing – original draft (supporting); Writing – review and editing (equal). **W. Wozniak:** Investigation (equal). **B. Kurowska:** Investigation (equal). **C. Bazioti:** Formal analysis (equal); Investigation (equal); Methodology (supporting); Validation (equal); Writing – original draft (supporting); Writing – review and editing (equal). **E. Guziewicz:** Funding acquisition (equal); Resources (equal); Supervision (lead); Validation (equal); Writing – original draft (supporting); Writing – review and editing (equal).

DATA AVAILABILITY

The data that support the findings of this study are available within the article.

REFERENCES

[1] C. Jagadish and S. J. Pearson, *Zinc Oxide Bulk, Thin Films and Nanostructures* (Elsevier, Oxford, 2006).

[2] K. Ellmer, A. Klein, and B. Rech, *Transparent Conductive Zinc Oxide* (Springer-Verlag, Berlin, 2008).

[3] S. Rajendran, J. Qin, F. Gracia, and E. Lichtfouse, *Metal and Metal Oxides for Energy and Electronics* (Springer Nature, 2021).

[4] R. Schifano, H. N. Riise, J. Z. Domagala, A. Y. Azarov, R. Ratajczak, E. V. Monakhov, V. Venkatachalapathy, L. Vines, K. S. Chan, J. Wong-Leung, and B. G. Svensson, "Comparison of the structural properties of Zn-face and O-face single crystal homoepitaxial ZnO epilayers grown by RF-magnetron sputtering," J. Appl. Phys. **121**, 015304 (2017).

[5] A. Bikowski and K. Ellmer, "A comparative study of electronic and structural properties of polycrystalline and epitaxial magnetron-sputtered ZnO:Al and $Zn_{1−x}Mg_xO$:Al films—Origin of the grain barrier traps," J. Appl. Phys. **114**, 063709 (2013).

[6] Ł. Wachnicki, T. Krajewski, G. Łuka, B. Witkowski, B. Kowalski, K. Kopalko, J. Z. Domagala, M. Guziewicz, M. Godlewski, and E. Guziewicz, "Monocrystalline zinc oxide films grown by atomic layer deposition," Thin Solid Films **518**, 4556–4559 (2010).

[7] P. Fons, K. Iwata, S. Niki, A. Yamada, and K. Matsubara, "Growth of high-quality epitaxial ZnO films on $\alpha−Al_2O_3$," J. Cryst. Growth **201-202**, 627–632 (1999).

[8] H. Kato, M. Sano, K. Miyamoto, and T. Yao, "Homoepitaxial growth of high-quality Zn-polar ZnO films by plasma-assisted molecular beam epitaxy," Jpn. J. Appl. Phys. **42**, L1002–L1005 (2003).

[9] R. Müller, F. Huber, M. Töws, M. Mangold, M. Madel, J. Scholz, A. Minkow, U. Herr, and K. Thonke, "High-quality ZnO layers grown by CVD on sapphire substrates with an AlN nucleation layer," Cryst. Growth Des. **20**, 3918–3926 (2020).

[10] J. Dai, H. Liu, W. Fang, L. Wang, Y. Pu, Y. Chen, and F. Jiang, "Atmospheric pressure MOCVD growth of high-quality ZnO films on GaN/Al_2O_3 templates," J. Cryst. Growth **283**, 93–99 (2005).

[11] R. Triboulet and J. Perrière, "Epitaxial growth of ZnO films," Prog. Cryst. Growth Charact. Mater. **47**, 65–138 (2003).

[12] V. Srikant, J. S. Speck, and D. R. Clarke, "Mosaic structure in epitaxial thin films having large lattice mismatch," J. Appl. Phys. **82**, 4286–4295 (1997).

[13] R. Chierchia, T. Böttcher, H. Heinke, S. Einfeldt, S. Figge, and D. Hommel, "Microstructure of heteroepitaxial GaN revealed by x-ray diffraction," J. Appl. Phys. **93**, 8918–8925 (2003).

[14] J. Faugier-Tovar, F. Lazar, C. Marichy, and C. Brylinski, "Influence of the lattice mismatch on the atomic ordering of ZnO grown by atomic layer deposition onto single crystal surfaces with variable mismatch (InP, GaAs, GaN, SiC)," Condens. Matter **2**, 3 (2017).

[15] See http://www.kymatech.com/ for more details on the substrate characteristics.

[16] E. Guziewicz, M. Godlewski, L. Wachnicki, T. A. Krajewski, G. Luka, S. Gieraltowska, R. Jakiela, A. Stonert, W. Lisowski, M. Krawczyk, J. W. Sobczak, and A. Jablonski, "ALD grown zinc oxide with controllable electrical properties," Semicond. Sci. Technol. **27**, 074011 (2012).

[17] S. Pung, K. Choy, X. Hou, and C. Shan, "Preferential growth of ZnO thin films by the atomic layer deposition technique," Nanotechnology **19**, 435609 (2008).

[18] S. Särkijärvi, S. Sintonen, F. Tuomisto, M. Bosund, S. Suihkonen, and H. Lipsanen, "Effect of growth temperature on the epitaxial growth of ZnO on GaN by ALD," J. Cryst. Growth **398**, 18–22 (2014).

[19] C. Thiandoume, V. Sallet, R. Triboulet, and O. Gorochov, "Decomposition kinetics of tertiarybutanol and diethylzinc used as precursor sources for the growth of ZnO," J. Cryst. Growth **311**, 1411–1415 (2009).

[20] See http://www.ammono.com/ for more details on the substrate characteristics.

[21] M. A. Moram and M. E. Vickers, "X-ray diffraction of III-nitrides," Rep. Prog. Phys. **72**, 036502 (2009).

[22] H. McMurdie, M. Morris, E. Evans, B. Paretzkin, W. Wong-Ng, L. Ettlinger, and C. Hubbard, Powder Diffr. **1**, 76 (1986).

[23] E. Guziewicz, M. Godlewski, T. A. Krajewski, Ł. Wachnicki, G. Łuka, J. Z. Domagała, W. Paszkowicz, B. J. Kowalski, B. S. Witkowski, A. Dużyńska, and A. Suchocki, "Zinc oxide grown by atomic layer deposition—A material for novel 3D electronics," Phys. Status Solidi B **247**, 1611–1615 (2010).

[24] K. Saito, K. Nagayama, Y. Hosokai, K. Ishida, and K. Takahashi, "Effects of GaN template on atomic-layer-epitaxy growth of ZnO," Phys. Status Solidi C **1**, 969–972 (2004).

[25] C. Lin, D. Ke, Y. Chao, L. Chang, M. Liang, and Y. Ho, "Atomic layer deposition of epitaxial ZnO on GaN and YSZ," J. Cryst. Growth **298**, 472–476 (2007).

[26] T. Metzger, R. Höpler, E. Born, O. Ambacher, M. Stutzmann, R. Stömmer, M. Schuster, H. Göbel, S. Christiansen, M. Albrecht, and H. P. Strunk, "Defect structure of epitaxial GaN films determined by transmission electron microscopy and triple-axis x-ray diffractometry," Philos. Mag. A **77**, 1013 (10251998).

[27]B. Fultz and J. Howe, *Transmission Electron Microscopy and Diffractometry of Materials* (Springer, Heidelberg, 2013).

[28]M. Birkholz, *Thin Films Analysis by X-Ray Scattering* (WILEY-VCH Verlag GmbH & Co., Weinheim, 2006).

[29]Th. De Keijser, E. J. Mittemeijer, and H. C. F. Rozendaal, "The determination of crystallite-size and lattice-strain parameters in conjunction with the profile-refinement method for the determination of crystal structures," J. Appl. Cryst. **16**, 309–316 (1983).

[30]R. Lee, A. M. West, A. A. Allerman, K. E. Waldrip, D. M. Follstaedt, P. P. Provencio, D. D. Koleske, and C. R. Abernathy, "Effect of threading dislocations on the Bragg peakwidths of GaN, AlGaN, and AlN heterolayers," Appl. Phys. Lett. **86**, 241904 (2005).

[31]O. Durand, A. Letoublon, D. J. Rogers, and F. H. Teherani, "Interpretation of the two-components observed in high resolution x-ray diffraction ω-scan peaks for mosaic ZnO thin films grown on c-sapphire substrates using pulsed laser deposition," Thin Solid Films **519**, 6369–6373 (2011).

[32]V. M. Kaganer, O. Brandt, A. Trampert, and K. H. Ploog, "X-ray diffraction peak profiles from threading dislocations in GaN epitaxial films," Phys. Rev. B **72**, 045423 (2005).

[33]M. A. Krivoglaz, *X-Ray and Neutron Diffraction in Nonideal Crystals* (Springer-Verlag, Berlin, 1996).

[34]M. Wilkens, "The determination of density and distribution of dislocations in deformed single crystals from broadened x-ray diffraction profiles," Phys. Status Solidi A **2**, 359–370 (1970).

[35]T. Yao and S.-K. Hong, *Oxide and Nitride Semiconductors Processing, Properties, and Applications* (Springer, Berlin, 2009).

[36]V. M. Kaganer, A. Shalimov, J. Bak-Misiuk, and K. H. Ploog, "Asymptotic x-ray scattering from highly mismatched epitaxial films," J. Phys.: Condens. Matter **18**, 5047 (2006).

[37]V. S. Kopp, V. M. Kaganer, M. V. Baidakova, W. V. Lundin, A. E. Nikolaev, E. V. Verkhovtceva, M. A. Yagovkina, and N. Cherkashin, "X-ray determination of threading dislocation densities in GaN/Al$_2$O$_3$(0001) films grown by metalorganic vapor phase epitaxy," J. Appl. Phys. **115**, 073507 (2014).

[38]N. Baddour and U. Chouinard, "Theory and operational rules for the discrete Hankel transform," J. Opt. Soc. Am. A **32**, 611–622 (2015).

[39]U. Chouinard and N. Baddour, "Matlab code for the discrete Hankel transform," J. Open Res. Softw. **5**, 4 (2017).

[40]I. Booker, L. R. Khoshroo, J. F. Woitok, V. Kaganer, C. Mauder, H. Behmenburg, J. Gruis, M. Heuken, H. Kalisch, and R. H. Jansen, "Dislocation density assessment via x-ray GaN rocking curve scans," Phys. Status Solidi C **7**, 1787 (2010).

[41]P. Gay, P. Hirsch, and A. Kelly, "The estimation of dislocation densities in metals from x-ray data," Acta Metall. **1**, 315 (1953).

[42]C. G. Dunn and E. F. Kogh, "Comparison of dislocation densities of primary and secondary recrystallization grains of Si-Fe," Acta Metall. **5**, 548 (1957).

[43]A. D. Kurtz, S. A. Kulin, and B. L. Averbach, "Effect of dislocations on the minority carrier lifetime in semiconductors," Phys. Rev. **101**, 1285 (1956).

[44]E. J. Mittemeijer and P. Scardi, *Diffraction Analysis of the Microstructure of Materials* (Springer-Verlag, Berlin, 2004).

[45]S. K. Mathis, A. E. Romanov, L. F. Chen, G. E. Beltz, W. Pompe, and J. S. Speck, "Modeling of threading dislocation reduction in growing GaN layers," J. Cryst. Growth **231**, 371 (2001).

[46]Y. Wang, X. L. Du, Z. X. Mei, Z. Q. Zeng, Q. Y. Xu, Q. K. Xue, and Z. Zhang, "Defect characteristics of ZnO film grown on (0001) sapphire with an ultrathin gallium wetting layer," J. Cryst. Growth **273**, 100 (2004).

[47]The theoretically expected inclination to the film normal of $\sim16°$ is determined by minimizing the strain energy expression [see Eq. (7) in Ref. 45] and by setting the ZnO Poisson ratio equal to 0.36. The latter is obtained using the elastic constant values reported in Ref. 48.

[48]Ü. Özgür, Ya. I. Alivov, C. Liu, A. Teke, M. A. Reshchikov, S. Doğan, V. Avrutin, S.-J. Cho, and H. Morkoç, "A comprehensive review of ZnO materials and devices," J. Appl. Phys. **98**, 041301 (2005).